A prototype 1 MeV X-band linac for aviation cargo inspection

M. Jenkins, G. Burt,* and A.V.Praveen Kumar[†]
Lancaster University Cockcroft Institute, UK

Y. Saveliev, P. Corlett, T. Hartnett, R. Smith, A. Wheelhouse, P McIntosh, and K Middleman
Sci-Tech Daresbury Laboratory, UK

Aviation cargo Unit Load Device (ULD) containers are typically much smaller than standard shipping containers, with a volume of around $1\,m^3$. Standard 3 to 6 MeV X-ray screening linacs have too much energy to obtain sufficient contrast when inspecting ULDs, hence a lower 1 MeV linac is required. In order to obtain a small physical footprint, which can be adapted to mobile platform applications, a compact design is required hence X-band radio frequency technology is the ideal solution. A prototype 1.45 MeV linac cavity optimised for this application has been designed by Lancaster University and STFC, manufactured by Comeb (Italy) and tested at Daresbury Laboratory using an e2v magnetron, modulator and electron gun. The cavity is a bi-periodic $\pi/2$ structure, with beam-pipe aperture coupling to simplify the manufacture at the expense of shunt impedance, while keeping the transverse size as small as possible. The design, manufacture and testing of this linac structure is presented. In order to optimise the image it is necessary to be able to modify the energy of the linac. It can be changed by altering the RF power from the magnetron but this also varies the magnetron frequency. By varying the beam current from 0-70 mA the beam energy varied from 1.45 to 1.2 MeV. This allows fast energy variation by altering the focus electrode bias voltage on the electron gun while keeping the dose rate constant by varying the repetition frequency. Varying the beam energy by varying the RF power and by varying the beam current are both studied experimentally. The momentum spread on the electron beam was between 1-5 % depending on the beam current of 0-70 mA

I. INTRODUCTION

Cargo at ports and airports are routinely scanned using X-rays to ensure their contents are consistent with the manifest [1]. These photons are typically generated by bremstrahlung using a linear accelerator. The cargo will either be driven through a portal or the linac will move along the cargo on a gantry such that a linear array of detectors can be utilised [4]. The frequency of aviation cargo Unit Load Device (ULD) container inspection is increasing due to security concerns. Due to the size of a ULD, typically $1\,m^3$, existing shipping cargo scanning linacs are unable to be used due to the high energy of the X-rays produced resulting in images with little contrast as the X-ray intensity varies very little with density due to the low attenuation of high energy X-rays. Current X-ray screening linacs were designed to scan shipping containers which are constructed from steel and have a volume of at least $33\,m^3$ which means that high energy X-rays (3-9 MeV) are required to traverse the container. ULD's are normally constructed from aluminium which combined with the much smaller volume of the container means that a lower energy linac with a beam energy of around $1-2\,MeV$ is required for sufficient contrast. As a mobile scanner is desired a compact design is necessary. The size and weight of a security linac is dominated by the shielding placed around the linac, which increases with linac diameter, which means that X-band RF technology, with its smaller transverse size, is ideal. A linac for cargo screening typically uses a long pulse electron gun, such that each pulse is a few thousand RF periods long. As a result the beam completely fills the longitudinal acceptance phase space, and not all the beam is captured. The linac is designed to have the synchronous phase vary along the first few cells to first capture and then accelerate the beam effectively. The capture efficiency is also dependant on the beam current due to space charge blow up. Prototyping of an X-band 1 MeV linac for security screening has been completed at STFC Daresbury Laboratory. This structure was manufactured by Comeb [2], Italy, and initial RF testing was conducted at the Cockcroft Institute. The linac was then installed on a beam line at Daresbury Laboratory to be tested using an e2v [3] magnetron, modulator and electron gun. In this paper we present the cavity design, ASTRA simulations of the beam-RF interaction, low power measurements of the cavity and finally measurements of the beam produced by the linac on a purpose built diagnostics line. In order to optimise the X-ray output to the cargo being scanned it is necessary to vary the linac energy and dose. The dose can be varied by simply changing the pulse repetition frequency or pulse duration. To vary the energy we can either vary the magnetron power or we can change the peak current from the gun to change the beamloading. Both methods will be investigated in this paper. We also present the energy spread of the beam

---

and the capture efficiency of the linac.

II. RF CAVITY DESIGN

For mobile cargo scanners the linac is normally mounted on a gantry or robot arm on the back of a truck. The weight on the rear axel of this truck is dominated by the mass of the shielding around the linac so keeping the outer diameter of the linac structure as small as possible is important. The cross sectional area of the shielding is given by the cross section of a hollow cylinder

$$Area = \pi(t^2 + 2rt) \tag{1}$$

where t is the shielding thickness and r is the inner radius of the shielding. Hence it is advantageous to have the cavity radius as small as possible. There are typically three frequency options for a security linac, S-band (3 GHz), C-band (6 GHz) and X-band (9.3 GHz) [5]. As size was a major consideration it was decided to use X-band, although other C-band would also be an option at the cost of additional shielding weight [6]. X-band technology was chosen to produce a physically small linac which not only ensures the linac is compact but the shielding is also compact. In order to increase the cavity stability a $\pi/2$ standing wave mode was selected, as this mode has the largest frequency separation between the operating mode and the next nearest mode which minimises the effect of cell geometry errors, due to finite mechanical tolerances, on the cavity field profile [7]. $\pi/2$ mode structures have every 2nd cell unfilled which could result in a much lower accelerating gradient if all cells were identical. A standard security linac structure utilises a side-coupled linac configuration where every 2nd cell is off-centre and is coupled to the cavity on either side via a slot in the equator of each cavity. In order to increase the accelerating gradient, which reduces the cavity length, while also keeping the outer diameter as small as possible a bi-periodic cavity design was chosen for this project, as shown in Fig. 1. The coupling cells in this configuration are on-axis, but every 2nd cell, known as the coupling cell, is much shorter in length than the other cells, known as the accelerating cells. Hence the outer diameter of the structure is not increased, but at the expence of a large spacing between the accelerating cells.

The energy of the electron beam adds extra complexity to the RF design. The electron gun which is connected to one end of the cavity produces $17\,\text{keV}$ electrons which are not fully relativistic. This means that the relativistic β of the electron beam changes along the length of the linac. Therefore the length of the accelerating cells, numbered 1 to n, increases along the length of the linac. The approximate length of cell n+1 is given by

$$L_{n+1} = \frac{v_n}{2f} + \frac{dv_n}{dz}\frac{L_{n+1}}{4f} \tag{2}$$

where v_n is the velocity of the electron entering cell $n+1$, and hence leaving cell n, and f is the frequency. Replac-
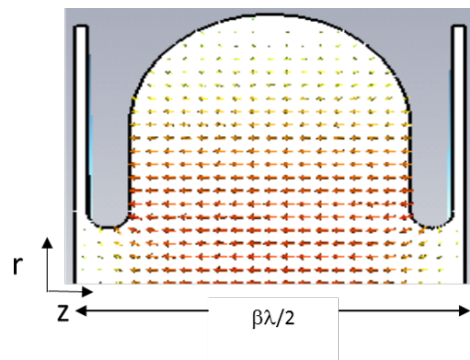
Figure 1. A single cell in a bi-periodic standing wave cavity, with the electric field.

ing v_n with β_n, which is the ratio of the particle velocity to the speed of light of the particle entering cell $n + 1$, we can rearrange equation (2) to

$$L_{n+1} = \frac{\beta_n}{\frac{2f}{c} - \frac{1}{2}\frac{\mathrm{d}\beta}{\mathrm{d}z}}. \tag{3}$$

The velocity gradient, $\mathrm{d}\beta/\mathrm{d}z$, is related to the accelerating gradient and chosen as a compromise between peak electric fields and the length of the structure to reach 1 MeV. It should be noted that due to relativity $\mathrm{d}\beta/\mathrm{d}z$ is not constant for a constant accelerating gradient and decreases to zero as the particles gain energy and the particle velocity tends to the speed of light.

An average gradient of 10 MV/m was chosen, a compromise between low probability of vacuum RF breakdowns without the need of extensive conditioning and minimising structure length, requiring 8 cells to reach 1 MeV. Cargo scanning linacs need to be made at lower manufacturing costs hence a low gradient will relax handling requirements during manufacture. At X-band the first 4 to 5 cells will be sub-relativistic and higher peak surface fields will be created in those cells if the peak on axis field is kept flat across all cells. While scientific linacs often operate at far higher gradient, commercial linacs often operate at much lower gradient with associated lower surface fields to reduce the processing required and to ensure that structures reach the desired field levels with high yields. The gradient will not be constant in each cell due to the large change in cell length. After the first cell the beam will form a bunch and we design the length of cells further downstream considering the interaction with the centre of this bunch and the RF. The phase difference between the RF phase seen by an electron in the centre of the bunch and the RF phase for maximum acceleration is known as the synchronous phase. A synchronous phase of 0 degrees results in maximum acceleration while a synchronous phase of -90 degrees results in maximum bunching. The synchronous phase will not be phased for maximum acceleration in the first few cells in order to increase capture and bunching, hence the exact cell length needs optimisation in a tracking code.

The power required to reach 1 MeV is around 300-500 kW which is lower than the power available from commercial pulsed X-band magnetrons (0.5-1.5 MW) hence the shunt impedance is not a major consideration. The optimisation hence focussed on minimising peak fields and minimising manufacturing complexity. The biperiodic cavity has a coupling-cell in between each accelerating cell hence the wall thickness is a key concern. A minimum thickness of 1.75 mm was chosen with a 1 mm coupling cell length as a compromise between structural integrity, manufacturing tolerances and peak fields. To simplify the manufacturing it was decided to couple the cells electrically through the beam aperture rather than magnetic coupling slots on the walls, this meant that nose cones (which would reduce the coupling factor) were not utilised on the cells except on the outer wall of the first cell.

The coupling factor, which is the bandwidth of the passband divided by the $\frac{\pi}{2}$ mode frequency, was chosen to keep the cavity fields equal in each accelerating cell, to minimise the field amplitude in the coupling cells, and to avoid any deviation of the phase advance per cell in the presence of manufacturing errors. The amplitude, A_{2n}, in the accelerating cell $2n$, with the coupler in cell $2m$, is given by

$$A_{2n} = (-1)^{n-m} A_{2m} \left[1 - \frac{2(m^2 - n^2)}{k^2 Q_a Q_c}\right] e^{\left(j\frac{4(m^2-n^2)}{k^2 Q_a}\frac{\Delta\omega}{\omega_a}\right)} \tag{4}$$

where Q_a is the Q of the accelerating cells, Q_c is the Q of the coupling cells, and $\Delta\omega$ is a frequency shift due to mechanical errors [7]. The beam aperture was chosen as a compromise between the cell-to-cell coupling factor and the peak surface fields, shown in Figure 2 for a $\beta = 0.7$ cavity. A peak surface electric field of 40 MV/m was chosen as a reasonable maximum for a commercial linac, hence for an accelerating gradient of 10 MV/m the maximum aperture radius of 5 mm was selected. This results in a coupling factor of 5 % which should be sufficient for an 8 accelerating cell cavity. A simple 8 accelerating cell cavity, if all cells were optimised for $\beta = 0.7$, would result in a amplitude drop of less than 0.3 % and a field in the coupling cell of less than 5 %, with a 50 micron manufacturing tolerance giving a phase shift of less than 2 degrees, while a 3 mm radius aperture would result in a 34 degree phase shift.

For linacs that bunch and accelerate electrons in a single structure the cell length is often given as a fraction of a a half free space wavelength, which is equivalent to the electron velocity β that would traverse the cavity without acceleration with the same phase at the entrance and exit, hence we refer to it as the cells β. In reality the electron velocity will vary across the cell length as it is accelerated, and some cells will be deliberately designed to be longer or shorter to provide a phase difference between cells to provide additional focussing, acceleration or bunching. For the first cell a β of around 0.3-0.5 is required, in order to capture the injected bunch. If a
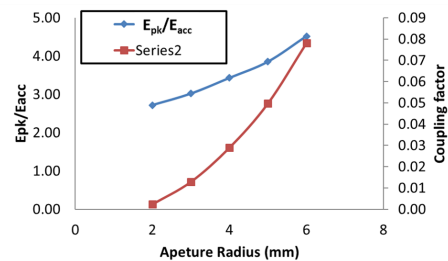
Figure 2. Ratio of peak electric field to accelerating field and coupling coefficient as a function of aperture radii for a $\beta=0.7$ cel

shorter cell is chosen the beam will enter the next cell in bunching phase, where as in a longer cell the bunch will enter the next cavity closer to the peak accelerating phase. Choosing the cell length allows an optimisation to be made to trade off beam capture efficiency and beam voltage. In order to optimise the length of each cell the equations of motion are solved for a on-axis single particle in the RF field. This neglects the effects of space charge in the initial optimisation but this will be considered later in the final optimisation. The RF longitudinal electric field field is assumed to be sinusoidal with a half period in each cell length, such that the cell length can be varied and optimised. The amplitude is set to a constant value in the last six cavities, the first two cavities are given an amplitude half the value of the other cells, as from experience the short length of these cells reduces the impedance causing these cells to have much smaller longitudinal electric fields on axis by around half. The cavity is split into a 1-D nodes, the time for the particle to reach the next node and the acceleration of the particle between the nodes is calculated. A particle is tracked to the end of the linac for different launch phases, and the phase of the RF when each particle reaches the interface between each cell is calculated. As we wish to minimise the linac's total length it was decided to bunch in the first two cells and then to be close to on crest for the last six cells. For maximum acceleration the electrons should enter and leave the cell at -90 degrees and +90 degrees respectively. For bunching the electron should leave the cell as a phase slightly greater than -90 degrees with maximum bunching/minimum acceleration at 0 degrees. To optimise the first two cell lengths we look at the exit phase of each cell as a function of launch phase, for different cell lengths considering a peak longitudinal field on axis of 25 MV/m. In Fig. 3 we can see that bunching is achieved around launch phases of -90 degrees because the exit phase is roughly constant for a large range of launch phases. The exit phase is a function of the cell length, with shorter cells having the bunch exit closer to 0 degrees providing more bunching but less acceleration. As the beam is injected at 17 keV the beam will likely experience high space charge forces if not accelerated in the first cell hence we have chosen to have the beam traverse the first cell in a time equivalent to a phase change

of 270 degree, entering at 0 degrees and leaving at -90 degrees for optimal acceleration in the 2nd cell, requiring a cell length of 5.5 mm, although this will be sensitive to the exact field profile in the final structure. It is noted that this doesn't result in the maximum capture as the bunch forms around launch phases of -90 degrees leaving the cavity at -54 degrees, however optimal capture of the bunch would require the phasing of the 2nd cavity to be 90 degrees off-crest. We would like the bunch to exit the 2nd cell at -90 degrees to get maximum acceleration in the last 6 cells. As can be seen in Fig. 4 for optimal acceleration of electrons launched at 0 degrees, where the first cell is 5.5 mm long the 2nd cell should be 7.5 mm long. It can be seen that the bunch is now forming around electrons launched at -50 degrees. We have chosen the 3rd cell to be slightly longer in order to provide a transverse RF focussing, the 4th cell is on crest, while all other cavities have a synchronous phase of around -10 degrees to maintain bunching throughout the linac. The final arrival phase functions for cells 1 and 2 are shown in Fig 5.
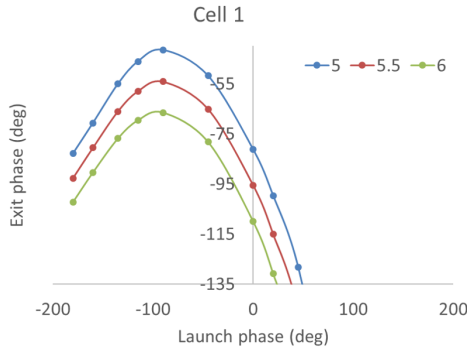
Figure 3. Arrival phase at the exit of the first cell as a function of the electron launch phase from the cathode, for differing lengths of the first cell
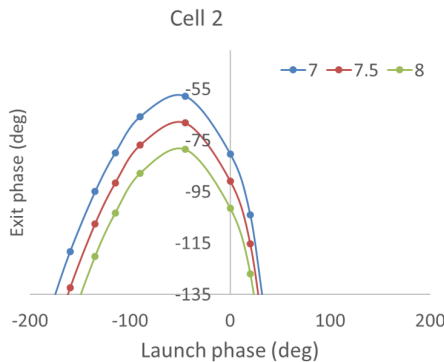
Figure 4. Arrival phase at the exit of the second cell as a function of the electron launch phase from the cathode, for differing lengths of the second cell

The structure is designed such that the particle at the
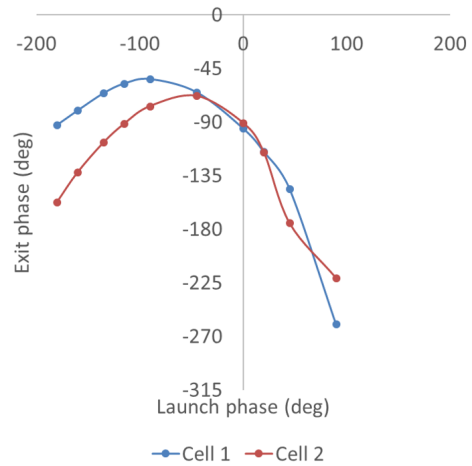
Figure 5. Arrival phase at the exit of the first and second cell as a function of the electron launch phase from the cathode for the optimised cell lengths
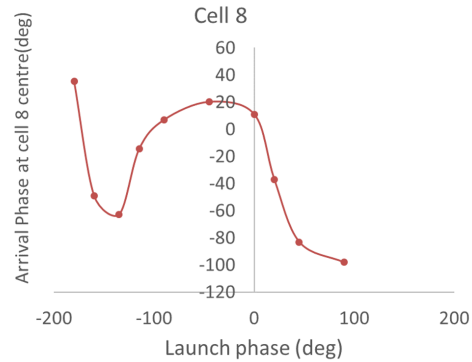
Figure 6. Arrival phase at the centre of the last cell as a function of the electron launch phase from the cathode
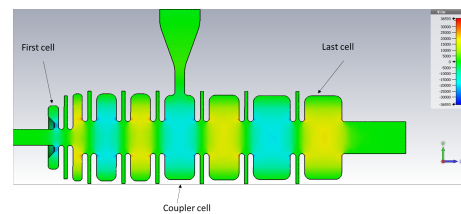
Figure 7. Image of the final linac design from CST after completion of the cell length optimisation

centre of the bunch leaving the first cavity is synchronised for maximum acceleration in the last six cavities, this particle is refereed to as the synchronous particle. The field experienced by the synchronous particle has been calculated from the on-axis field from CST and is shown in Figure 8 for a 1.1 MeV beam, again using the equations of motion in a simple 1D tracking calculation. The phase in the first cell is not set for maximum acceleration and is set to around -30 degrees to provide

bunching as well as acceleration. The synchronous particle does not traverse the first cavity 90 degrees out of phase with the longitudinal electric field as one would expect as the low injection energy, of 17 MeV would mean that many decelerated particles would be reflected back to the electron gun. The small deceleration slows down the initial particles without reflecting them allowing later particles to catch up at an early stage allowing a greater beam capture. The cavity phase is adjusted to 20 degrees in the last cell at the design energy in order to provide some transverse focussing at the linac exit, by lengthening the next to last cell, as shown in Fig 6 which shows the phase that each electron arrives at the centre of the last cell as a function of its launch phase, showing most particle launched between -100 degrees and 0 degrees arrive close to the design phase. The final design requires some adjustment to account for the field decay in the beam pipe. The synchronous fields seen by the beam in the final design are shown in Fig 8. The final design achieved sufficient bunching for the beam output energy to have a fairly broad maxima as shown in Figure 9. At the injection end of the linac the beam velocity is low and hence the combined length of the accelerating and coupling cavities must be very short to maintain synchronism. The optimum cavity design will have the smallest possible wall thickness and coupling cell length without compromising the ability to manufacture the cavity, and hence these will not vary as the cell length varies with particle velocity. As the wall thickness and the coupling cell length do not decrease with particle velocity, the accelerating cell length must be very short. The short cell length adds two issues, the fields become weak on axis, as the fields decay rapidly across the beam aperture due to the divergence of the electric field, and the cell becomes mechanically stiff making frequency tuning more difficult. In an initial prototype the first cell could not be tuned due to this mechanical stiffness. To resolve these issues a smaller aperture radius of 2.5 mm was chosen for this cell to increase the field on axis, and nose cones were added to the cell such that a larger cell equator could be utilised with a small gap to enable tuning of this cell. The nose cones do however result in a higher peak surface electric field in this cell and a lower peak electric field on axis but it was felt that the ability to tune this cell was critical. While using a side-coupled structure would alleviate this problem it would require a larger transverse structure size and hence was not chosen. Alternatively a higher injection energy could be utilised in future versions if the peak fields in the first cell were found to cause issues when conditioning the cavity. The coupler has been added to a middle cell to reduce the effect of manufacturing tolerances on the phase and amplitude shift of the cavity from the ideal values, and hence the distance from the coupler to the furthest cell is minimised, as can be seen from equation 4. The final structure after optimisation of the cell lengths is shown in Figure 7, and the high surface electric field in the first cell can clearly be seen. The accelerating cell lengths are shown in Table I.

The final cavity size became very compact with a length of 10.4 cm (13.5 cm flange to flange) and a 49 mm diameter.

Table I. Accelerating cell lengths.

Cell No.	Cell Length
Cell 1	5.806 mm
Cell 2	7.419 mm
Cell 3, 4	10.645 mm
Cell 5, 6	13.871 mm
Cell 7	16.129 mm
Cell 8	13.379 mm
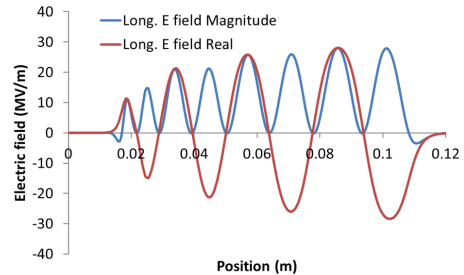
Figure 8. Plot of the magnitide of the longitudinal electric field on axis in the cavity and the synchronous field seen by the electron beam.
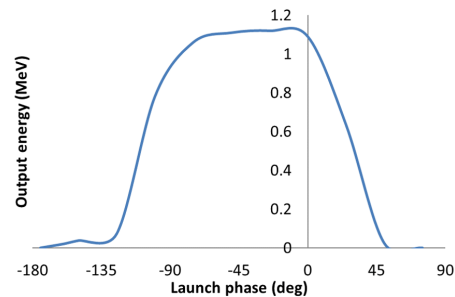
Figure 9. Plot of the electron beam energy as a function of the launch phase

In order to calculate the required power it was necessary to calculate the structure impedance. As the electron velocity, and hence gradient, varies the transit time factor is not a constant hence the definition of shunt impedance that doesn't include the transit time factor was used. As the phase in each accelerating cell varies by 180 degrees from each of its neighbouring accelerating cells, it was necessary to define the voltage, V, as the integral of the magnitude of the electric field rather than the real part to avoid cancellation as given in equation 5. This means that the impedance, Z, is

$$Z = \frac{V^2}{P} = \frac{(\int |E_z| dz)^2}{P} \tag{5}$$

where P is the power lost in the cavity walls, and E_z is the longitudinal electric field.

In addition to the shunt impedance the optimisation also considered the peak surface electric field, E_{peak}, and the peak surface magnetic field, B_{peak}, normalised by the maximum on axis electric field, E_{max}. For the final structure, after the cell length optimisation, the impedance and peak surface fields are shown in Table II

Table II. Cavity parameters

Frequency	9.3	GHz
Impedance, Z	6.97	$M\Omega$
$\frac{E_{peak}}{E_{max}}$	1.79	
$\frac{B_{peak}}{E_{max}}$	3.38	$\frac{mT}{m}$
Q_o, Q_e	7328	
No. of cells	8	
Structure length	10.4	cm
Smallest aperture	5	mm
Nominal input power	500	kW
Nominal max E field on axis	27	$\frac{MV}{m}$

III. BEAM DYNAMICS SIMULATIONS

In order to include space charge, ASTRA was used to track particles through the cavity. These simulations were used to further optimise the length of each cell. A file containing the input beam phase space at the exit of the electron gun was provided by the electron gun manufacturer, e2v. The 17 keV input beam had a spot size of $\sigma_x = 0.15$ mm and a correlated transverse momentum with a maximum of $p_x/p_z = -8$ mrad, and was injected 15 mm away from the cavity. The energy spectrum of the bunch at the cavity exit for a maximum on-axis electric field of 28 MV/m is shown in figure 10, for 300,000 tracked macroparticles. An aperture radius of 2.5 mm was applied in the simulations from the cathode at z=0 until 20 mm into the cavity at z=35 mm at the exit of the first cell, it then increases to 5 mm in the rest of the cavity, as can be seen in 7, up to z=140 mm and then increases again to 10 mm in the beamline up to z=600 mm, which was the beam pipe aperture after the structure used in the experiment, was used in the simulations to remove any lost electrons.

As can be seen in fig. 10, the electron energy distribution has a peak at 1.10 MeV and a long tail of lower energy electrons and a small tail of higher energy electrons. The capture of the beam is strongly dependent on the field in the cavity as sufficient field is required to bunch the beam at the linac entrance. This means that at low field the beam is not synchronously accelerated and there is a drop in maximum beam energy at the output as can be seen in Fig. 11. Using the simulation of a 1.10 MeV beam the RF power required to maintain this field at zero current was calculated using the modified shunt impedance definition from earlier calculated
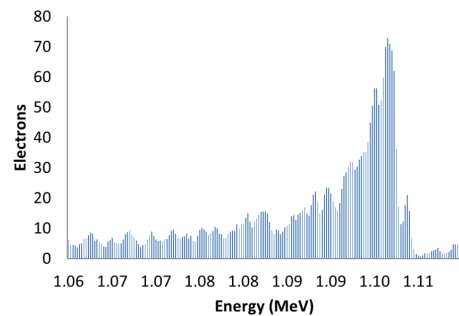
Figure 10. Energy spectrum of the beam at the cavity output from ASTRA

in CST, equation 5 and a rough approximation for the additional power required for a finite beam current due to beamloading by multiplying the current by the beam energy to give the total power required as shown in Fig. 12.
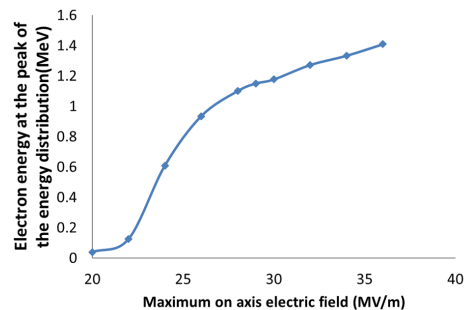
Figure 11. Peak energy as a function of maximum electric field on axis from ASTRA
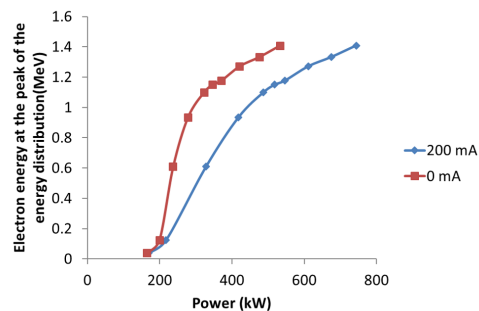
Figure 12. Peak energy as a function of power using shunt impedance and beam loading

Space charge forces within the bunch can also affect the capture of the electron bunch as shown in Fig. 13, here capture is defined as the percentage of electrons that reach the linac exit. The maximum capture at very low current is 70 % by calculating the current at the exit divided by the input beam current, in ASTRA while one may expect the maximum capture is 50 % from Fig 9

where only around 50 % of initial launch phases are accelerated to high energy, the ASTRA simulations show a long low energy tail which exit the linac without hitting a wall. As the current increases this low energy tail expands and is removed by the aperture reducing capture. The beam phase space 75 cm downstream after the cathode is shown in Fig. 14.
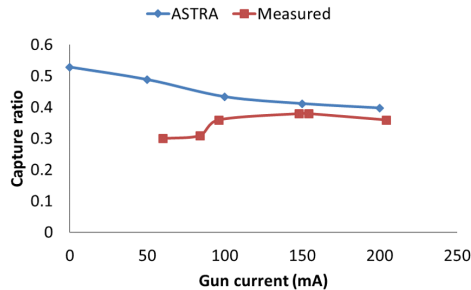
Figure 13. Beam capture ratio as a function of the DC current from the electron gun
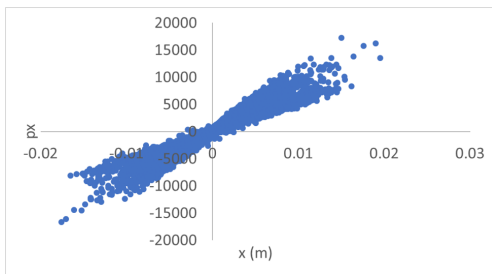
Figure 14. Transverse phase space of the beam 75 cm downstream from the cathode

IV. LOW POWER CAVITY TESTING

The cavity was manufactured by Comeb in Italy from OFHC copper by diamond turning and vacuum brazing. When the cavity was received from Comeb it was measured using a bead pull system. The bead pull was done using a non-resonant method[11] as it is faster than the resonant method, only reflection could be measured as the cavity did not have a pick-up and so the measurements were performed using S_{11}. The initial measurement made upon receiving the cavity was to measure S_{11} and compare with the S_{11} measurements provided by Comeb as well as the expected S_{11} from simulations of the cavity. Figure 15 shows the results of the S_{11} measurements performed.

The S_{11} minimum of the operating mode agrees well with the measurements performed at Comeb and at the Cockcroft Institute. Table III compares the frequency and match of the operating mode measurements with the expected values from CST.
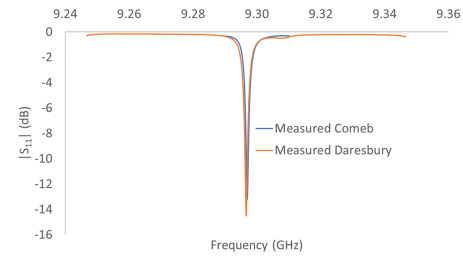
Figure 15. Magnitude of S_{11} for the X-band cavity. The S_{11} measurement performed by the manufacturer is shown in blue and the S_{11} measurement performed on receipt of the cavity is shown in orange.

Table III. S11 measurement of the operating mode.

	Units	CST	Measured
Frequency	GHz	9.29743	9.29696
S_{11} minima	dB	-11.5539	-13.1971
Q_o minima		7328	8123
Q_e minima		7328	11980
Nearest mode Δf	MHz	83.4	91.1

Figure 16 shows the initial bead pull result compared with the predicted field profile for the cavity calculated using CST. The data has been normalised so that the peak electric field is set to 1. The measured data agrees very well with the predicted data except in the first two accelerating cells. There are three peaks in the measured data where we would only expect two peaks. This could mean that there is electric field in the first coupling cell which means that the actual field is a superposition of the modes with phase advance per cell of π, $\pi/2$ or 0. If the phase change between the cells is not $\pi/2$ this has implications for the quality of the electron beam.
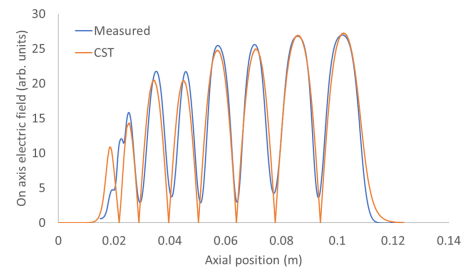
Figure 16. Field profile plot showing how the electric field varies along the axis of the cavity. The orange line shows the measured field profileafter tuning and the blue line the expected field profile.

To attempt to correct the field in the first two accelerating cells a tuning procedure was started based on simulations by introducing errors to the cell radii to attempt to replicate the measured field profile. The tuning methodology used was a modified version of the tuning method developed for the SPARC RF deflector[12]. The method had to be modified as the deflector was tuned

using the H field whilst for the this linac we tuned using the E field. Using this method on the measured field profile using coefficients obtained from CST simulations predicted that the largest error was in the first accelerating cell so this was tuned first. The tuning resulted in an unexpected change in the field profile. It was expected that the peak in the coupling cell between the peaks corresponding to the first two accelerating cells would reduce. Instead it has increased to a point where it is level with the field in the second accelerating cell. We stopt tuning of the structure as we are unsure of the phase of each cell and hence the tuning could be making the field profile worse. There is also a concern that due to the finite bead size and the small coupling cell width the measured field in that cell will have large errors.

V. BEAM CHARACTERISATION

A. Experimental layout and beam diagnostics

Following the low level RF testing of the cavity it was installed in the Linac Test Facility (LTF) at Daresbury Laboratory. The electron gun, magnetron and modulator were obtained from e2v. The electron gun is a 17 keV, 200 mA DC gun with an incorporated focus electrode that can be used to modulate the emission to provide the pulsed beams required for the linac. The emission is cut-off when the focus electrode potential drops 1.5 kV with respect to the cathode. The magnetron was the MG6005 tunable x-band magnetron from e2v, capable of producing 1.3 MW at a duty cycle of 0.0008. In order to fully characterise the beam the tungsten bremsstrahlung target was designed to be removable to allow the beam to be injected into a diagnostics line. The experimental layout that includes basic beam diagnostic systems is shown in Fig. 17. The beam current was measured by an Integrating Current Transformer (ICT) at the linac exit and by a Faraday Cup (FC) at the end of the beamline straight. In addition, the current delivered to the cathode of the linac thermionic gun was evaluated by a current transformer outside the experimental beamline. These three independent measurements allow to evaluate capture efficiency represented by the ratio of ICT to cathode current I_{ICT}/I_{cath} and "transmission efficiency" represented by the ratio of FC to ICT current I_{FC}/I_{ICT}. The distance between ICT and FC was 1.7 m with minimal vacuum aperture of 38 mm. Transverse beam dynamics was investigated with two phosphor screens on metal substrates S1 and S2. These allow to measure transverse beam size and distribution, and evaluate the beam divergence. A horizontal insertable slit located alongside the screen S1 in combination with screen S2 were used for estimating the vertical transverse emittance of the electron beam. Note that the diagnostic unit with S1 screen contained also a tungsten target for X-ray generation but it was not employed in these experiments.

The beam energy and energy spectra were measured
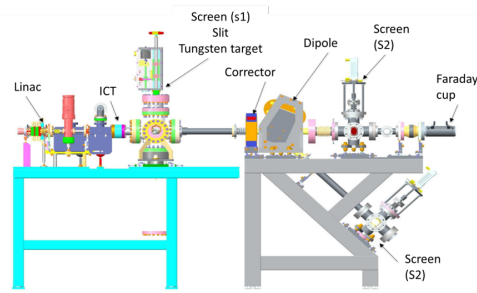
Figure 17. Experimental layout with beam diagnostics. The overall length of the beamline from the linac gun to the Faraday cup is 2.3m.

in the energy spectrometer comprising of the dipole magnet and screen S3 and with slit in S1 position inserted. The dipole magnetic field was mapped to provide accurate beam energy measurements from the dipole current. The dipole used in this setup was of sector bend type thus providing transverse focusing in a bend plane. The distances slit-to-dipole and dipole-to-S3 were chosen such that to image slit onto screen S3 thus minimising contribution of the transverse beam size to energy spectra measurements. The dispersion of 0.6 m on screen S3 was evaluated by simulations.

The main two variables in the experiments presented here were (i) the cathode current corresponding to the beam current at the exit from the linac of up to 70 mA and (ii) the RF power to the cavity of up to 520 kW.

B. Transverse beam dynamics

At nominal beam energy above 1.3MeV, the beam transverse size and beam divergence depend weakly on the average beam current. Within beam current range of $I_{ICT} = 3 - 76$ mA, the horizontal beam RMS sizes on screens S1 and S2 were $\sigma_{1h} = 2.8 \pm 0.4mm$ and $\sigma_{2h} = 4.0 \pm 0.3mm$ and the vertical beam sizes were $\sigma_{1v} = 3.6 \pm 1.1$ mm and $\sigma_{2v} = 4.6 \pm 0.2$ mm. Typical beam images on screens S1 and S2 and corresponding beam profiles are shown in Fig. 18 for the case of the beam current $I_{ICT} = 49$ mA. Note the beam is always larger in vertical direction compared to horizontal one. This may be an indication of some azimuthal field non-symmetry within the linac. The beam divergence between screens S1 and S2 was crudely estimated as

$$x' = \frac{(\sigma_2 - \sigma_1)}{L} \tag{6}$$

where L is a distance between S1 and S2 giving 1.0 ± 0.1 $mrad$ in both horizontal and vertical planes. Assuming the above beam divergence, the beam size at the exit from the linac can be extrapolated as roughly 2.6 mm RMS.

With decreasing RF power in the cavity, the beam transverse size increased and the overall beam quality de-
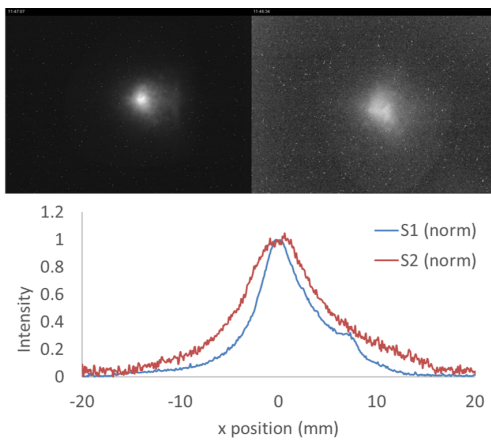
Figure 18. Beam images on screens S1 and S2 and corresponding transverse beam profiles.

graded significantly. This was not investigated in detail due to difficulties in quantitative interpretation of beam images but is illustrated by the capture and transmission efficiencies (as described above) presented in Figure 19.
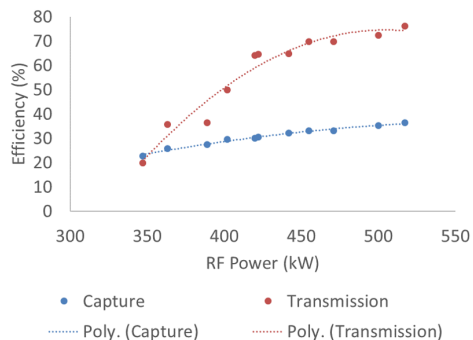
Figure 19. Capture and transmission efficiencies versus linac RF power.

Transverse emittance was estimated at 1.3 MeV beam energy by collecting beam images on screen S1 and slit images on screen S2. No strong evidence of the dependence of the emittance on beam current was found that could be explained, in part, by shot-to-shot beam parameters variation. Within the range of beam currents $I_{ICT} = 10 - 60 \ mA$, the average RMS normalised emittance was measured $\epsilon = 6.8 \pm 0.8 \ mm.mrad$ compared to $\epsilon = 7.3 \ mm.mrad$ predicted by ASTRA.

C. Beam energy and spectra

The beam energy depends on linac RF power and beam current as expected and is shown in Figure 20. The RF power here is given as a difference between forward and reverse power measurements. The plot presents experimental data only for the range of RF power investigated

and on linear scale for clarity. The same data if plotted as the beam energy vs square root of RF power give a linear fit with accurate extrapolation to zero according to

$$\text{Beam energy (eV)} = 1943.2\sqrt{\text{RF power}} \qquad (7)$$

The maximal beam energy achieved from the linac tested was 1.42 MeV with an energy spread of 1.45 % at 520kW of the linac RF power and a beam current of 11.6 mA. However changing the output power of a magnetron also changes the frequency of the magnetron by a few MHz, known as frequency pushing, and the frequency of the cavity varies due to the change in heating hence an auto frequency tuner is required to keep the magnetron frequency equal to the cavity frequency under all circumstances. The auto frequency tuner measures the reflection mid-pulse and adjusts a tuning stub on the magnetron to minimise the reflection. Beam loading in the linac is an important factor affecting the achievable beam energy as demonstrated in Figure 21. The maximum beam energy at the exit from the linac decreases by approximately 15% when the beam current changes from a few mA to 70 mA. Decreasing the beam energy via beam loading by increasing the beam current has the downside that the dose is also increased which requires the pulse repetition frequency or duration to be decreased to compensate. Energy spectra exhibit a relatively well defined high energy peak and a long low energy tail as expected from simulations(Figure 22). The high energy peak widens with increasing beam current (Figure 23) that can be attributed to space charge effects. The image at S3 of the energy tail was outside the momentum acceptance of the analyser system and it was not possible to stitch together the partial spectra and reconstruct the whole spectrum due to beam jitter, caused by the pulse to pulse variation in the magnetron output. To quantify the energy spectra as a function of the beam current, the FWHM energy spread in the main peak was measured and presented in Figure 23. It is noted that the measured energy spread was partly attributed to non-flat top feature of the RF pulse as shown in Figure 24. Over the 2.5 μs long pulse, the RF power into the cavity varies by approximately 20-25 kW. With reference to the dependence of the beam energy on RF power (Figure 20), this translates to 2% variation of relative beam momentum which is larger than predicted by ASTRA. Since the current pulse from the thermionic gun is longer than the RF pulse, this effect should be a contributing factor to observed energy spectra (Figure 22) and measured energy spreads (Figure 23) as the beam will see a varying voltage as the cavity fills.

VI. CONCLUSION

A bi-periodic $\pi/2$ mode structure has been developed at the Cockcroft Institute, Daresbury Laboratory by Lancaster University, STFC ASTeC and Technology Depart-
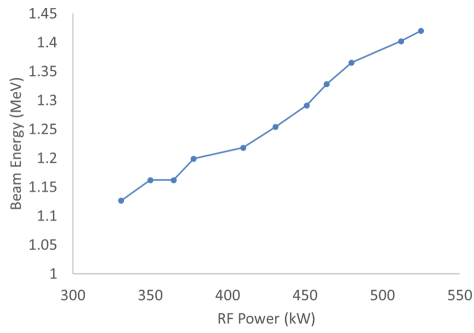
Figure 20. Beam energy as a function of the linac RF power.
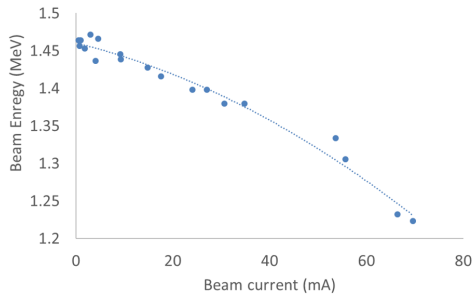
Figure 21. Beam energy as a function of beam current
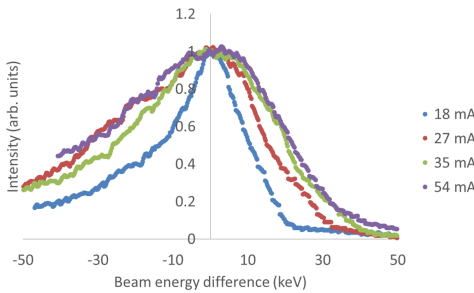
Figure 22. Energy distribution of the beam energy spectra main peak at four beam currents.
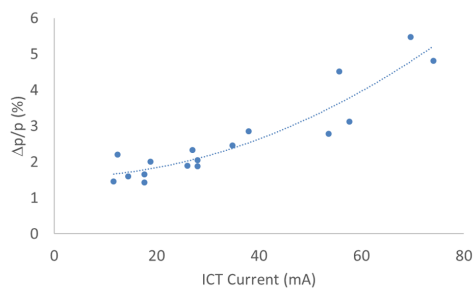
Figure 23. Relative beam momentum spread of the beam spectra main peak as a function of the beam current.

ments for use in security scanning applications. The cavity is very compact with a length of 10.4 cm (13.5 cm
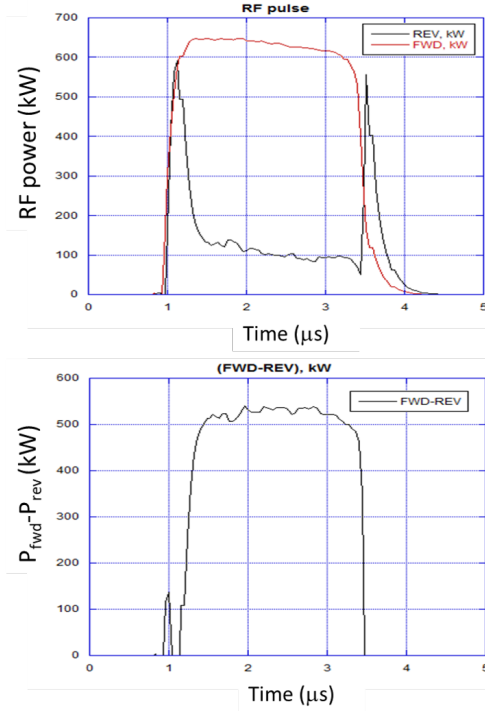
Figure 24. (a) Linac forward and reverse RF power traces ; (b) difference between the two.

flange to flange) and a 49 mm diameter. The cavity has been received from the manufacturer and after initial testing and tuning of the structure was installed on a beam line. The electron beam produced by the linac was characterised before being used to produce X-rays for security scanning. The linac is able to vary its maximum beam energy between 1.15 MeV to 1.45 MeV by varying either the magnetron power or the beam loading. If the variation is performed by the RF power a linac capture efficiency of 20-40 % is obtained. If the beam current is varied space charge forces result in a momentum spread of 2-5 % depending on the beam current. The larger energy range is obtained by varying the RF power however this also varies the magnetron frequency, and hence the slow mechanical auto-frequency tuner needs to adjust the magnetron frequency to remain constant. By varying the beam current and repetition frequency the energy can be varied faster and more stably as the change in cavity frequency will be slower than the auto-frequency tuner.

[1] Zentai, George. "X-ray imaging for homeland security." International Journal of Signal and Imaging Systems Engineering 3, no. 1 (2010): 13-20.

[2] Comeb, italy, http://www.comeb.it/

[3] e2v, Chelmsford, UK, https://www.e2v.com/

[4] Wronka, Sawomir. Interlaced Energy Linac with Smooth Energy Regulation. No. CERN-ACC-2016-0060. 2016

[5] Tang, Ch, H. Chen, Y. Liu, and X. Wang. "Low-energy linacs and their applications in Tsinghua University." In Proceedings of LINAC, pp. 256-258. 2006.

[6] Shao, Jiahang, Yingchao Du, Hao Zha, Jiaru Shi, Qiang Gao, Qingxiu Jin, Huaibi Chen et al. "Development of a C-band 6 MeV standing-wave linear accelerator." Physical Review Special Topics-Accelerators and Beams 16, no. 9 (2013): 090102.

[7] Wangler, Thomas P. RF Linear accelerators. John Wiley & Sons, 2008.

[8] ASTRA, DESY, http://www.desy.de/~mpyflo/

[9] CST Microwave Studio, CST GmbH, Germany, http://www.cst.com/

[10] G. Burt et al., "Design and Operation of a Compact 1 MeV X-band Linac", MOPB004, Proceedings of LINAC12, Tel-Aviv, Isreal (2012).

[11] A. Mostacci et al., "About Non Resonant Perturbation Field Measurment in Standing Wave Cavities", TH5PFP086, Proceedings of PAC09, Vancouver, BC, Canada (2009).

[12] L. Ficcadenti et al., "RF Measurements Results of the Final Brazed SPARC RF Deflector", FRPMN030, Proceedings of PAC07, Albuquerque, New Mexico, USA (2007).